Acta Metallurgica Sinica (English Letters) (2021) 34:963–972
https://doi.org/10.1007/s40195-020-01184-z

Formation Mechanism of Nanoparticles in Fe–Cr–Al ODS Alloy Fabricated by Direct Oxidation Method

Fuzhao Yan[1,2] · Jing Li[1] · Yiyi Li[1] · Liangyin Xiong[1] · Shi Liu[1]

Received: 21 July 2020 / Revised: 3 September 2020 / Accepted: 10 October 2020 / Published online: 7 January 2021
© The Chinese Society for Metals (CSM) and Springer-Verlag GmbH Germany, part of Springer Nature 2021

Abstract
This study presents the fabrication of 14Cr Fe–Cr–Al oxide dispersion strengthened (ODS) alloy by a direct oxidation process. In order to explain how oxide nanoparticles are formed in the consolidation process, the powders after oxidation are subjected to vacuum thermal treatment at high temperatures. Differential scanning calorimeter, X-ray photoelectron spectroscopy, scanning electron microscopy and transmission electron microscopy techniques are used to detect the generation, evolution of oxides on both the surface and interior of the powder, as well as the type of oxide nanoparticles in the fabricated ODS alloy. It is found that an iron oxide layer is formed on the surface of the powder during low temperature oxidation. And the iron oxide layer would be decomposed after thermal treatment at high temperature. In the consolidation process, the oxygen required by the reaction of alumina and yttrium oxide to produce nanoscale Y–Al–O particles mainly derives from the decomposition of iron oxide layer at elevated temperature and the inward diffusion of oxygen. Using the direct oxidation process, $YAlO_3$ nanoparticles are dispersed in the grains and at the grain boundaries of Fe–Cr–Al ODS alloy.

Keywords Fe–Cr–Al ODS alloy · Direct oxidation · Iron oxide layer · Y–Al–O nanoparticles · Formation mechanism

1 Introduction

Oxide dispersion strengthened (ODS) alloy demonstrates high creep strength, high stability at elevated temperature and good irradiation resistance [1, 2]. In addition, ODS alloy with appropriate amount of aluminum exhibits excellent high temperature corrosion resistance [3, 4]. Therefore, Fe–Cr–Al ODS alloy has become a research hotspot of candidate structural materials for fusion and fission reactors in the future [5, 6]. Their outstanding behavior is inseparable from the existence of dispersed thermally stable Y–Al–O nanoparticles, which act as pinning points to inhibit dislocation movement, retard recovery and recrystallization processes [7, 8].

In the conventional fabrication of ODS alloys, mechanical ball milling with yttria particles is an indispensable process to introduce oxygen content. After that, the mechanically alloyed (MA) powders are consolidated into alloy by hot extrusion (HE) or hot isostatic pressing (HIPing). However, there are several unavoidable shortcomings during MA process, such as introducing more impurities [9], low efficiency, variance of batch production [10] and uncontrollable increases in oxygen or carbon [11]. To avoid MA process, many oxidation methods have been proposed and developed. In the fabrication of Fe–Cr ODS alloy, Rieken et al. [12] used reactive atomization gas to oxidize Fe–Cr powder surface during atomization process. They found that a metastable Cr-enriched oxide layer was formed and transported oxygen into the interior of powder and alloy, to contribute the generation of Y–Ti–O nanoparticles. Based on the same principle, Gil et al. [13, 14] developed surface treatment of gas atomized powder followed by reactive synthesis (STARS) to make Fe–Cr ODS alloys. The metastable oxide layer was also obtained which acted as oxygen reservoirs. However, the effective generation

Available online at http://link.springer.com/journal/40195

✉ Jing Li
jingli@imr.ac.cn

✉ Shi Liu
sliu@imr.ac.cn

1 Materials for Special Environments Division, CAS Key Laboratory of Nuclear Materials and Safety Assessment, Shi-changxu Innovation Center for Advanced Materials, Institute of Metal Research, Chinese Academy of Sciences, Shenyang 110016, China

2 School of Materials Science and Engineering, University of Science and Technology of China, Shenyang 110016, China

of Y–Al–O nanoparticles cannot be guaranteed by using the above two methods. It is due to the fact that the dense Al_2O_3 film is easily formed on the surface of Fe–Cr–Al powder under the high temperature environment of gas atomization, preventing the inward migration of oxygen and the reaction of aluminum oxide and yttrium oxide. More recently, Li et al. [15] put forward a process of vacuum heat treatment followed by slow oxidation to prevent the formation of alumina film on the Fe–Cr–Al powder surface. The Y–Al complex nanoscale oxides were generated in the Fe–Cr–Al matrix, and the mechanical strength was improved. Unfortunately, it is a lengthy oxidation process.

In this study, a simple direct oxidation method is proposed to fabricate 14Cr Fe–Cr–Al ODS alloy. The practicability of this new method for fabrication of ODS alloy is analyzed. The oxide chemistry during the fabrication and formation mechanism of Y–Al–O nanoparticles is elucidated.

2 Experimental

Fe–Cr–Al powder containing Y, Al and Ti was produced by plasma rotating electrode process (PREP). The composition of atomized powder is listed in Table 1, and the particle size of the selected powder was less than 53 μm. On the premise of accurately controlling the oxygen pressure of 20 Pa, the Fe–Cr–Al powders were directly heat-treated at a low temperature of 300 °C for 24 h. The oxygen content in the powders was increased from 0.018 to 0.1 wt% during the oxidation treatment. The resulting oxidized powder was named as 14Cr-A. After degassing and vacuum-sealing, powder 14Cr-A was consolidated into ferritic alloy by HIPing at 1150 °C for 3 h. In order to simulate the change of oxide dispersoids in ferritic powder with temperature changing during HIPing consolidation, powder 14Cr-A was vacuum heat-treated at 800 °C and 1150 °C for 3 h, respectively. Then the obtained powders were named as 14Cr-B and 14Cr-C.

Powder 14Cr-A was tested by differential scanning calorimeter (DSC) on a simultaneous thermal analyzer NETZSCH STA449F3. The powder was heated up to 1300 °C at a heating rate of 10 °C/min in a high purity Ar atmosphere. The flow rate is about 30 ml/min. The surface composition of oxidized and as-vacuumed powder was obtained by X-ray photoelectron spectroscopy (XPS) on a Thermal Scientific ESCALAB 250 spectrometer using a monochromatic source of X-ray Al *K*α. All binding energies of the XPS spectra were referenced to C 1*s* peak of 284.6 eV. Since the analysis area was considered to be planar, no correction for the spherical shape of the powder was introduced. The evolution of chemical composition in depth was measured by argon ion beam etching using a sputtering rate of 0.1 nm/s. The surface microstructure of oxidized and as-vacuumed powders was examined by field emission scanning electron microscope (FE-SEM) using a Zeiss Sigma 500 with an energy dispersive X-ray spectroscopy (EDS) analyzer. The nanometric features in the as-HIPed alloy were characterized by two transmission electron microscopes, FEI Tecnai G2 20 (TEM) and FEI Tecnai F20 (HRTEM) equipped with EDS, at an accelerating voltage of 200 kV. TEM specimens were electro-polished by a TENUPOL 5 twin-jet polisher using a solution containing 10 vol% $HClO_4$ and 90 vol% CH_3OH. The microhardness of as-HIPed alloy was measured on a MICROMET 5103 Vickers hardness tester using Vickers diamond pyramid indentation with a load of 500 g. The hardness value was obtained by the average of 10 consecutive indentations.

Table 1 Chemical composition of the atomized powder (wt%)

Powder	Fe	Cr	Al	Y	Ti
Fe–Cr–Al	Bal.	13.95	4.16	0.47	0.55

3 Results

3.1 Microstructure of Powder 14Cr-A

The morphology, size and distribution of oxide dispersoids on the surface of powder 14Cr-A under different magnification is shown in Fig. 1. The entire powder surface is oxidized at 300 °C. A number of oxide islands are generated on the surface of the powder, and some dispersoids with large size are preferentially located near the grain boundaries, forming continuous chains. EDS analysis was used to check the composition of dispersoids in the grains and near the grain boundaries in Fig. 1b. The composition of different points is listed in Table 2. Compared with the position of point 2 in the grain, the higher contents of Ti, Al, Y and O near the grain boundaries are identified. In the research of Permalloy (nominally 81 at%Ni + 19 at%Fe) thin film diffusion couples, Miller and Gangulee [16] have observed the volume diffusion of Ti at 200–350 °C, which gave rise to the change of various physical properties. The volume diffusion of Al into polycrystalline Si at temperature of 300 °C has also been evidenced by Nakamura and Kamoshida [17]. In comparison with volume diffusion, the activation energy of grain boundary diffusion is expected to be relatively small and consequently the diffusion rate is relatively fast. Therefore, the diffusion of Ti and Al along the grain boundary to the surface of these ferritic powders can take place under the long-term oxidation. As for Y, having a large ion size, bulk (volume) diffusion is not easy to realize [18]. Grain boundaries and defects become the preferentially sites for outward diffusion and migration [19]. Accordingly, the concentration of Y near the grain boundaries in the present investigation is higher than that of the matrix.

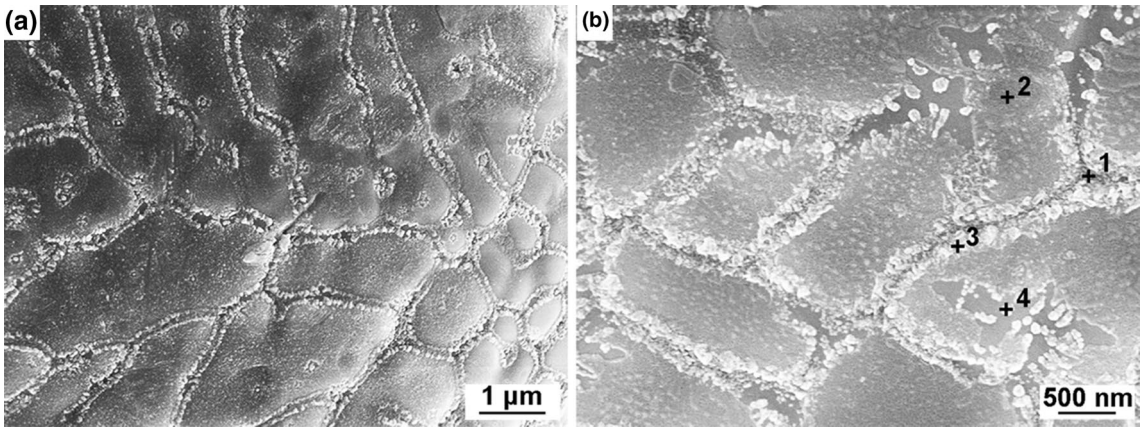

Fig. 1 SEM images of dispersoids on the surface of powder 14Cr-A under **a** low, **b** high magnifications

Table 2 Composition of the surface of powder 14Cr-A (wt%)

Point	Fe	Cr	Al	Y	Ti	O
1	71.7	15.0	6.2	2.0	1.3	3.8
2	79.90	14.11	4.22	0.1	0	1.67
3	75.52	14.94	4.33	1.10	1.01	3.1
4	74.7	14.71	5.69	0.01	0.67	4.22

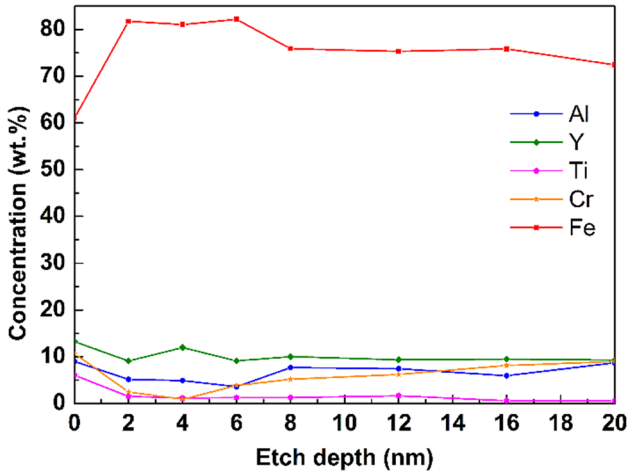

Fig. 2 Auger electron spectroscopy (AES) depth profile of surface chemical composition of the powder 14Cr-A

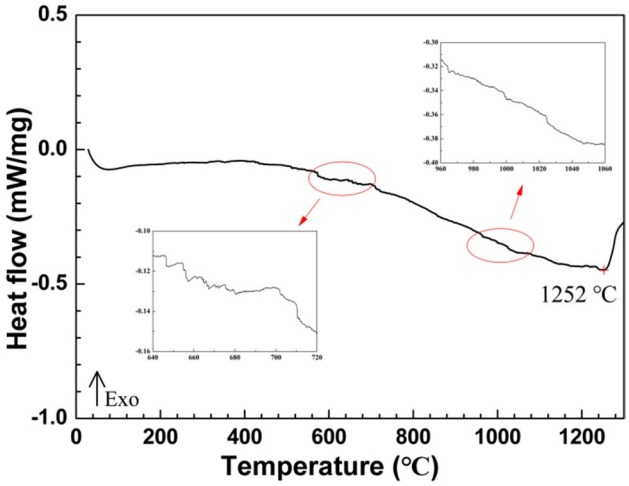

Fig. 3 DSC curve of the oxidized powder 14Cr-A

Figure 2 shows the element change near the surface of powder 14Cr-A. In order to facilitate comparison with matrix elements, the calculated element content is based on the removal of O. Although the enrichment of Ti and Y concomitant with the depletion of Fe and Cr is obtained in the surface layer within 2 nm of powder 14Cr-A, iron oxide accounts for a relatively high proportion near the surface.

DSC result of the powder 14Cr-A is shown in Fig. 3. The continuous change peaks from 640 to 720 °C and around 1000 °C (marked with red circles) on DSC curve appeared. It indicates a series of oxide composition changes occur during the heating of these powders. Also, it suggests that these oxidized powders in this temperature range do not undergo a simple exothermic reaction. For this reason, the powder 14Cr-A was again vacuum treated at 800 °C and 1150 °C, respectively, to simulate and explain the transformation of oxidized powder in the consolidated process. It should be noted that 1150 °C is the sintering temperature of HIPing process.

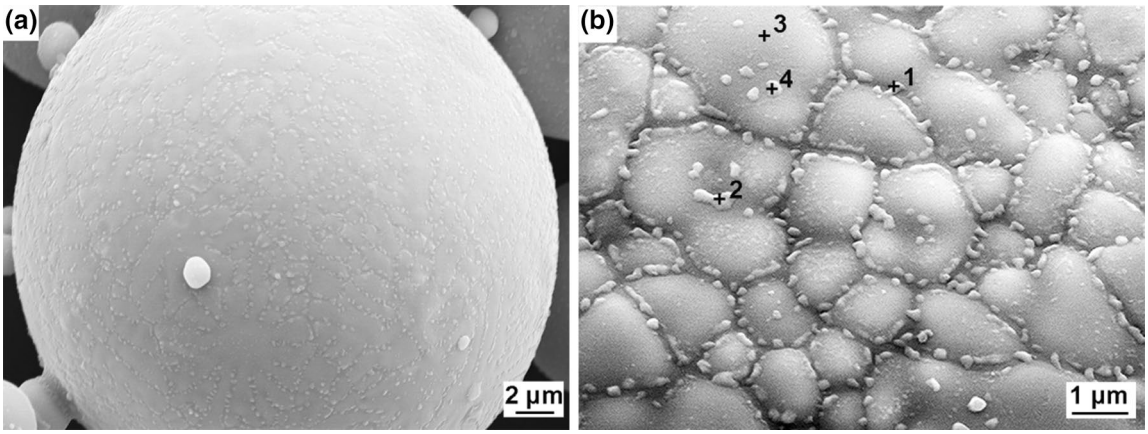

Fig. 4 SEM images of dispersoids on the surface of powder 14Cr-B under **a** low, **b** high magnifications

Table 3 Composition of the surface of powder 14Cr-B (wt%)

Point	Fe	Cr	Al	Y	Ti	O
1	75.0	11.1	7.9	2.3	0.5	3.2
2	76.2	13.2	5.7	0	0.8	4.1
3	78.9	13.3	5.8	0.1	0.2	1.7
4	78.8	11.7	6.8	0	0.5	2.2

3.2 Microstructures of Powder 14Cr-B and 14Cr-C

After thermal treatment at 800 °C for 3 h in a vacuum environment, the surface morphologies of powder 14Cr-B are shown in Fig. 4. The oxide islands in the grains become denser, and the surface become smoother. The continuous oxide chains located near the grain boundaries on the powder surface in Fig. 1b have become the small intermittent lumps as shown in Fig. 4b. These small intermittent lumps seem to mainly cover the outer layer of the denser oxide islands along the grain boundaries. Table 3 lists the composition of four different points in Fig. 4b. An increase in aluminum contents is observed at all points, concomitant with a decrease in chromium content and an increase in yttrium content at some points. In the XPS results of Fig. 5, the concentration of aluminum and yttrium near the surface (in the range of 6 nm) of 14Cr-B has a significant improvement compared with the surface of powder 14Cr-A (in Fig. 2). Consistent with the studies of surface segregation in austenitic stainless steel and MCrAlY alloys [20–22], the grain boundary migration of aluminum and yttrium to the surface of powder 14Cr-B is favored at elevated temperature. Meanwhile, the concentration enrichment of aluminum and yttrium leads to the evident depletion of iron content on the surface. The oxygen concentration on the lumps is higher than that on the smooth island (point 3), indicating the strong oxygen affinity of active elements, e.g., Y and Al.

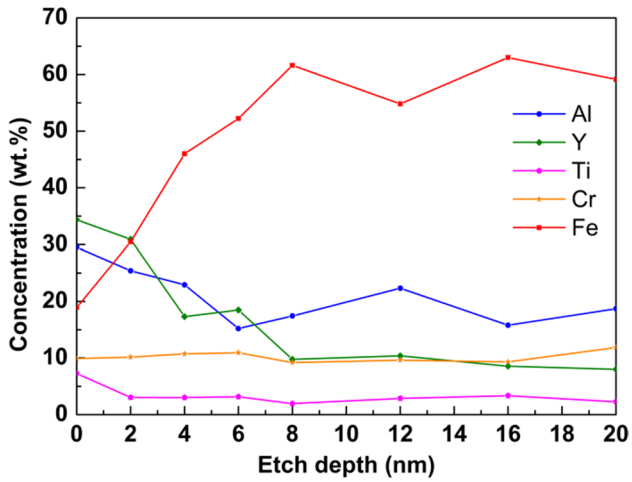

Fig. 5 AES depth profile of surface chemical composition of powder 14Cr-B

Figure 6 displays the surface oxide morphology of powder 14Cr-C after vacuum heat treatment at 1150 °C. A rigid shell has been developed on the powder surface, leading to a fuzzy distinction between grain boundaries and grains. Several small cubes with dimension close to or lower than micron are left on the surface of the shell. The composition result of different points is listed in Table 4. It is found that the iron content on the surface decreases sharply, as the temperature is increasing. Comparatively, the depletion

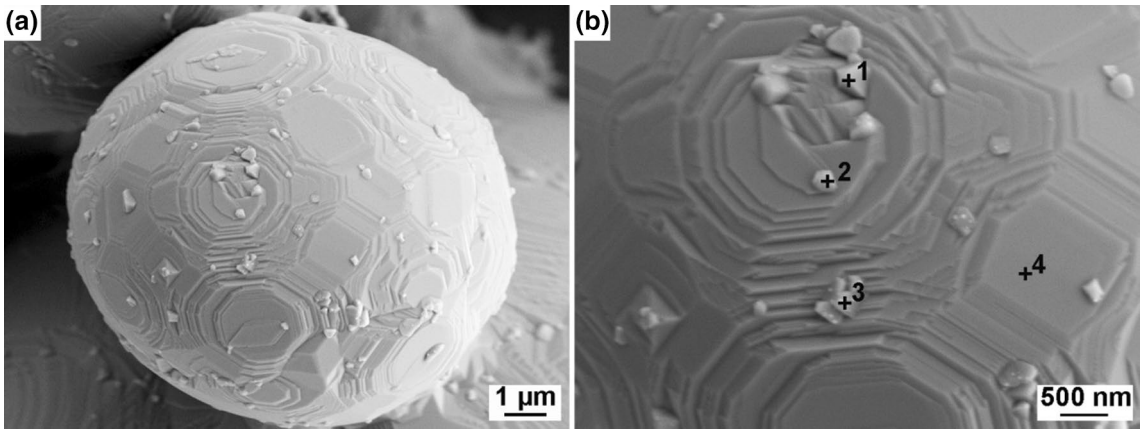

Fig. 6 SEM images of dispersoids on the surface of powder 14Cr-C under **a** low, **b** high magnifications

Table 4 Composition of the surface of powder 14Cr-C (wt%)

Point	Fe	Cr	Al	Y	Ti	O
1	43.2	10.5	21.1	0.6	0.2	24.4
2	54.7	11.9	17.4	0	0.4	15.6
3	53.5	11.4	16.8	1.4	0.3	16.6
4	55.4	12.6	15.7	0.1	0.3	15.9

of Cr is small. The enrichment of Al on the surface significantly exceeds that of powder 14Cr-A and 14Cr-B. Also, the segregation of Y on some grain boundaries is detected. In this study, the heat treatment is carried out in a vacuum environment. However, a certain amount of oxygen is contained in powder 14Cr-A. Accordingly, the stoichiometric composition of Al_2O_3 can be attained when temperature is over 1000 °C, as evidenced in Ref. [23].

The XPS result in Fig. 7 shows that the aluminum oxide is the predominant in a depth of tens of nanometers beneath the surface of powder 14Cr-C. The shell and the small cubes at 1150 °C are mainly composed of aluminum oxides.

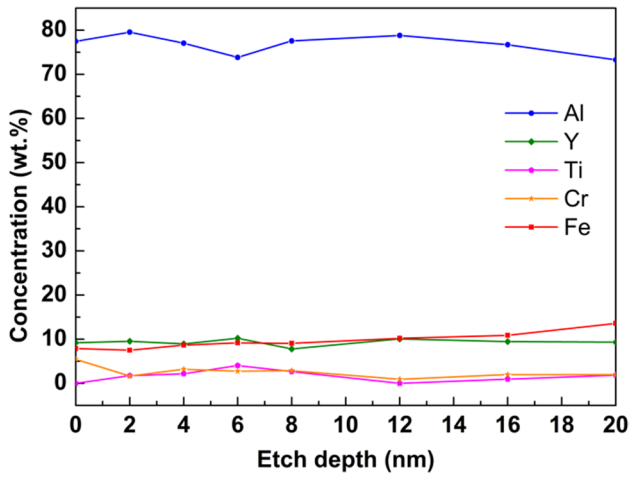

Fig. 7 AES depth profile of surface chemical composition of powder 14Cr-C

3.3 TEM Analysis of as-HIPed Alloy

TEM is used to observe the distribution and morphology of nanoscale oxide particles in the as-HIPed alloy, and the result is shown in Figs. 8 and 9. As shown in Fig. 8a, a large number of nanoscale particles are dispersed in the specimen. The size of nanoparticles varies from no less than 10 nm to a maximum of 170 nm. Almost 95% of oxide nanoparticles are concentrated in the size range of 10–40 nm as shown in Fig. 8b, which is within the size range of nanoparticle fabricated by MA method. Based on an assumption that the thickness of TEM foil is 50 nm, the number density of oxide nanoparticles in the as-HIPed alloy is calculated to be 5.18×10^{21} m^{-3}. It is higher than that of 16Cr Fe–Cr–Al ODS alloy fabricated by internal oxidation method [15], but lower than that fabricated by MA method [24], under the same assumption.

Figure 8c shows the chemical composition of the largest particle (marked 1) in Fig. 8a. It is mainly composed of Al-enriched oxide. This is apart from the result obtained by Li et al. [15] that the large particles were composed of Y_2O_3 after the two-step oxidation process to fabricate 16Cr Fe–Cr–Al ODS alloy. It is speculated that oxidation

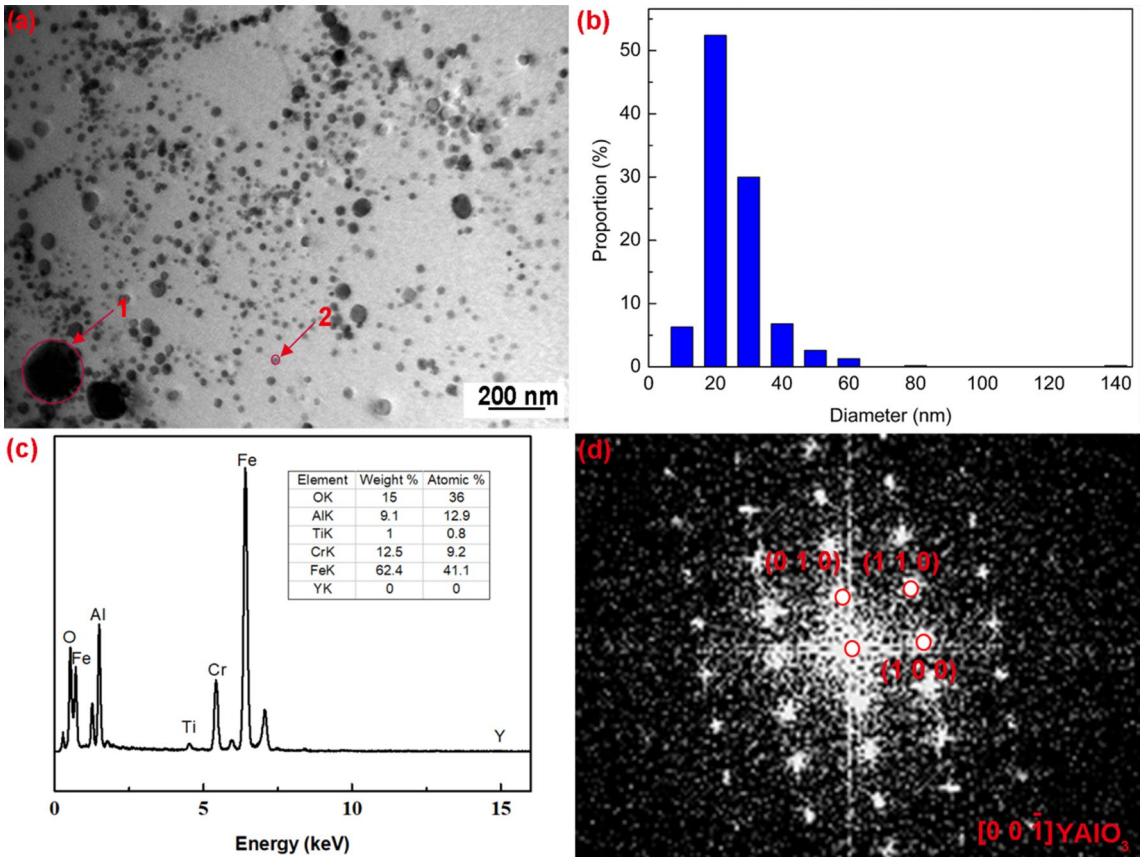

Fig. 8 TEM/HRTEM results of the as-HIPed alloy: **a** bright field image of nanoparticles, **b** particle size distribution of nanoparticles, **c** EDS energy spectrum and composition of particle 1 in **a**, **d** FFT pattern of particle 2 in **a**

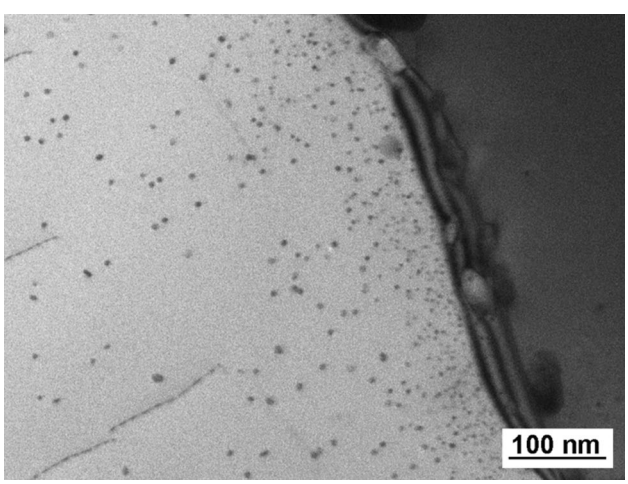

Fig. 9 TEM bright field image of oxide particles near grain boundary

process is a crucial parameter to change composition of nanoscale oxide.

Diffraction pattern of a small particle (~25 nm, marked 2) from fast Fourier transformation (FFT) is shown in Fig. 8d. The measured values of inter-planar distances (d) and angles (α) from the reciprocal space are consistent with that of $YAlO_3$ phase with an orthorhombic structure (PDF: #33-0041), and they are listed in Table 5 (the electron beam is paralleled to [00$\bar{1}$] zone axis of this particle). As such, Y–Al–O complex nanoparticles are generated in this direct oxidation method. In this investigation, no particle of Y_2O_3 and TiO_2 is distinguished by HRTEM.

Table 5 Inter-planar spacing (d) and angles (α) of particle 2 and the possible indexing

d (Å), α (°)	d_1 (011)	d_2 (121)	d_3 (110)	α_{12}	α_{23}
Measured	5.357	4.469	7.135	35.48	54.58
$YAlO_3$	5.329	4.318	7.137	35.86	54.14

In this investigation, the mircohardness of as-HIPed specimen is 275.2 ± 10 $Hv_{0.5}$. The result is slightly reduced in comparison with the value of 291–304 $Hv_{0.5}$ on as-HIPed FeCrAl ODS specimen manufactured by MA method [25]. It can be explained by the lack of strain hardening that is usually produced during mechanical ball milling. Compared to the value of 137 $Hv_{0.5}$ and 180 $Hv_{0.1}$ in ODS alloys fabricated by gas atomization oxidation method [12, 14], the

microhardness of as-HIPed alloy is significantly improved. It indicates the good compactness of Fe–Cr–Al ODS alloy and the considerable number of oxide nanoparticles in the matrix.

On the other hand, the heterogeneous distribution of oxide nanoparticles in some regions is also observed, as shown in Fig. 9. The number density of particles decreases with the increasing distance from grain boundary. The specific reason will be discussed in the next chapter.

4 Discussion

Detail high-resolution XPS spectra of powder alloy elements after different heat treatments are presented in Fig. 10. Obviously, the oxygen peaks near the powder surface are mainly rooted in the contribution of metal oxides (O^{2-}, 532–530 eV) under all the conditions. Nevertheless, the peak position shift of about 0.38 eV indicates that the element combined with oxygen has changed from iron element to aluminum or/and yttrium element with the change of heat treatment. For iron and chromium, the peaks of powder 14Cr-A in Fig. 10a appear at 710.4 eV and 576.6 eV, respectively, which can be explain by the fact that these two elements have been oxidized at a certain depth near the powder surface. And iron is concentrated on the outermost surface, and chromium is presented in the inner oxide layers. Such phenomenon is coincident with the oxidation results of SUS 304 and 316 in air below 500 °C [26]. By studying thin oxide films formed on Fe-*X*Cr ($X = 10$, 30, 50, 70 and 90 mass%) alloys at 600 °C in air, Kosaka et al. [27] obtained that chromium oxide was predominant in the oxide film only when the chromium content was more than 50%. In the present investigation, the oxidation temperature and the chromium content have been reduced. Consequently, the content of iron oxide should be much higher than that of chromium oxide, and the predominant oxide on the surface of powder 14Cr-A is a thin iron oxide layer. After vacuum heat treatment at 800 °C, i.e., on the surface of 14Cr-B powder, the oxidic peaks of Fe and Cr disappeared and only metallic peaks are remained, which indicates that oxygen combined with them at low temperature (300 °C) has been transferred. As the temperature increases, no strong peaks of iron and chromium near the surface were detected in Fig. 10c, due to the outward diffusion and enrichment of aluminum and yttrium. The weak metallic peak of iron and the strong oxidic peaks of aluminum and yttrium at 1150 °C give evidence that the oxygen transferred from iron has combined with aluminum and yttrium, because of the strong oxygen affinity of both the elements. At elevated temperature, the aluminum oxides are dominating at the etching depth within 20 nm of powder. Based on the refined spectrum of each element, it can be concluded that the oxygen in powder 14Cr-A has diffused from iron oxide and small amounts of chromium oxide to aluminum and yttrium elements under high temperature and vacuum environment. It is different from the previous studies of Rieken and Gil et al. [12–14] that a metastable Cr-enriched oxide layer was the carrier to transport oxygen in the fabrication of ODS-FeCr alloy. Authors deem that oxidation temperature in this direct oxidation method is the main reason. High temperature favors the formation of thermodynamically stable phase, such as Cr_2O_3. Whereas, low temperature kinetics favors the formation of an iron oxides layer [28]. Therefore, in this investigation iron oxide is the main oxygen reservoir due to its high bulk concentration and provides oxygen for the formation of Y–Al–O nanoparticles during HIPing consolidation of high temperature and vacuum.

It is well acknowledged that synthesizing Y–Al–O compounds from the oxides Y_2O_3 and Al_2O_3 under normal pressure require a relatively high temperature (≥ 1600 °C) [29]. But under the action of high pressure, the synthesis temperature will drop below 1000 °C [30]. According to the powder analysis, it obtained that aluminum and yttrium would diffuse to the grain boundaries and the surface of powder under vacuum condition at elevated temperature. And they will combine with oxygen transferred from iron and the minor chromium, being the reactive substances for synthesis reaction. Meanwhile, the high external compressed force in HIPing process causes the powder surface to be broken and the grain boundary to be twisted. The powder surface and grain boundary enriched with Y, and Al becomes the preferential sites for formation of Y–Al complex oxides. Therefore, high density Y–Al–O nanoscale particles are easy to precipitate near the grain boundary, as shown in Fig. 9.

To further elucidate the precipitation process of oxide nanoparticles in direct oxidation method, a schematic diagram of oxide dispersoids decomposition and complex nanoparticle re-precipitation during the oxidation and HIPing process is displayed in Fig. 11. Firstly, a large number of islands and a layer mainly composed of iron oxide are formed at the surface of the powder after direction oxidation treatment. After being vacuum-packaged, the powder in the container is heated under high external stress. With the increase of temperature, the composition of oxide island changes. The islands mainly composed of iron oxide in Fig. 11a are transformed into aluminum and yttrium oxide in Fig. 11b owing to the outward diffusion and strong oxygen affinity of Al and Y. Under the synergistic effect of stress and element diffusion, the metastable iron oxide layer on the powder surface is thinned and decomposed. Simultaneously, the high temperature and pressure facilitate the chemical reaction of alumina and yttrium oxide to form complex Y–Al oxides nanoparticles.

In the study of PM2000 ODS alloy, Dawson showed that the lowest temperature of nanoscale oxides precipitation

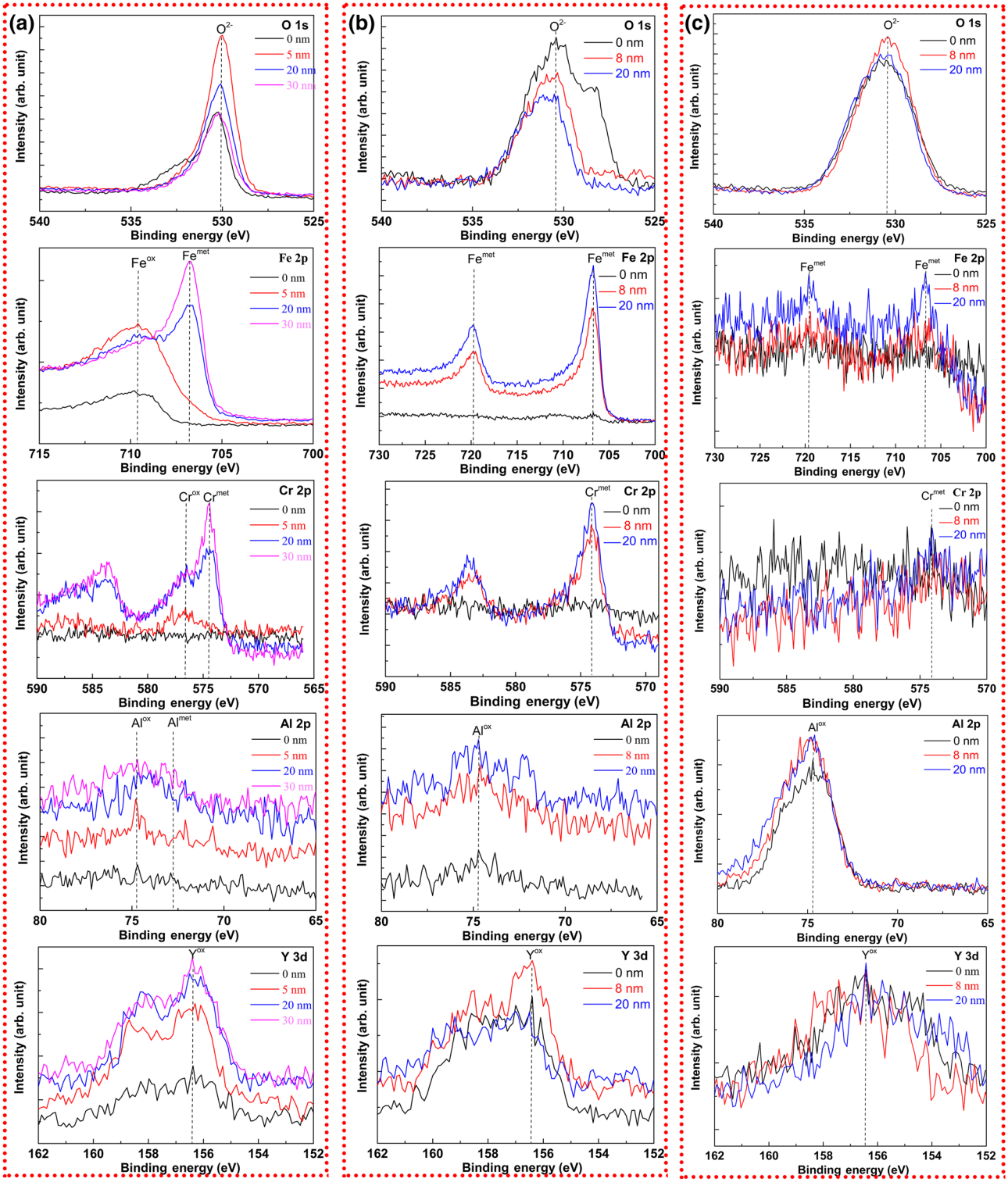

Fig. 10 Detailed XPS spectra of oxygen, iron, chromium, aluminum and yttrium near the surfaces of **a** 14Cr-A, **b** 14Cr-B, **c** 14Cr-C

is 650 °C [31]. The precipitation of oxides is not directly observed in the present investigation; however, some oxide nanoparticles should nucleate with the rising temperature. Being the reactive substance for synthesis reaction, the content of alumina is relatively high, which leads to large particle of aluminum oxides remaining in ODS alloy as shown

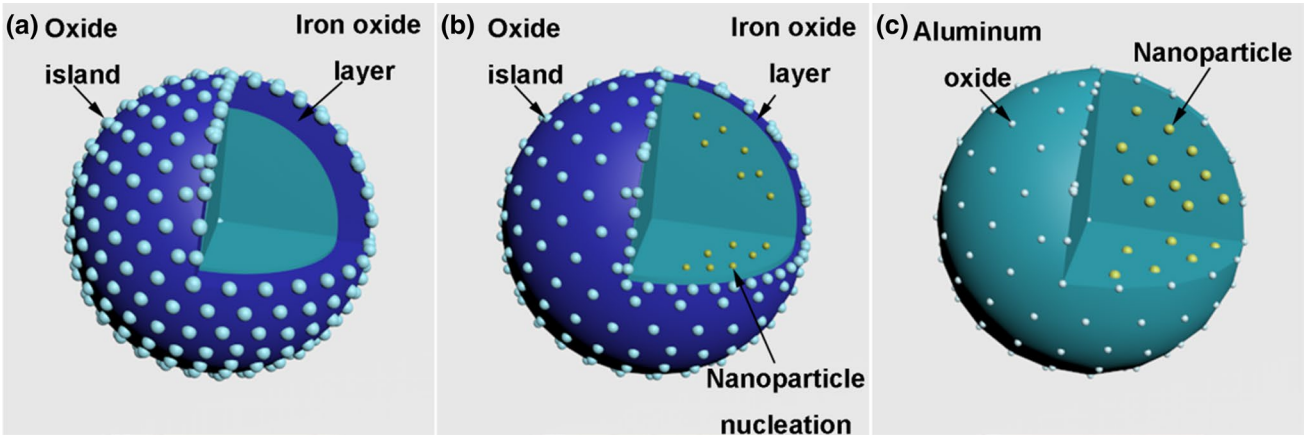

Fig. 11 Schematic diagram for the formation process of oxide nanoparticles: **a** after direct oxidation, **b** during heating, **c** after HIPing. For illustrative purposes, a small amount of chromium oxide on the surface is ignored

in Fig. 8c. In this investigation, the iron oxide layer obtained from direct oxidation at low temperature becomes the oxygen reservoir in the powder consolidation. The oxygen diffusion from iron oxide layer to aluminum and yttrium provides a potential for the successfully formation of Y–Al–O nanoparticles.

5 Conclusions

In this study, a simple direct oxidation method was proposed to fabricate Fe–14Cr–4.2Al–0.5Ti–0.5Y Fe–Cr–Al ODS alloy. A wide variety of analytical techniques involve in XPS, SEM, DSC and TEM were utilized to characterize the surface feature and transformation process during heating of the oxidized powder and the distribution of oxide nanoparticles in the ODS alloy. The following main results were obtained:

1. After oxidation at 300 °C in 20 Pa O_2, a thin oxide layer mainly composed of iron oxide was formed on the surface of the powder. A small amount of Al, Y and Ti were enriched at the grain boundary.
2. Vacuum heat treatment at high temperature resulted in the decomposition of metastable iron oxide layer. Simultaneously, the oxygen combined with iron was transferred and bonded to aluminum and yttrium, due to the outward migration and strong oxygen affinity of aluminum and yttrium.
3. High temperature and high external compressed force promoted the reaction of aluminum and yttrium oxides to produce Y–Al–O nanoparticles. In some region of the ODS alloy, the number density of oxide nanoparticles near grain boundaries was higher than that in grains.

Acknowledgements This work was supported by the National Defense Science and Technology Industry Nuclear Material Technology Innovation Center Project (No. ICNM-2020-ZH-17).

References

[1] T. Allen, J. Busby, M. Meyer, D. Petti, Mater. Today **13**, 14 (2010)
[2] S.K. Karak, T. Chudoba, Z. Witczak, W. Lojkowski, I. Manna, Mater. Sci. Eng. A **528**, 7475 (2011)
[3] P. Dou, A. Kimura, T. Okuda, M. Inoue, S. Ukai, S. Ohnuki, T. Fujisawa, F. Abe, Acta Mater. **59**, 992 (2011)
[4] A. Kimura, R. Kasada, N. Iwata, H. Kishimoto, C.H. Zhang, J. Isselin, P. Dou, J.H. Lee, N. Muthukumar, T. Okuda, M. Inoue, S. Ukai, S. Ohnuki, T. Fujisawa, T.F. Abe, J. Nucl. Mater. **417**, 176 (2011)
[5] H. Shibata, S. Ukai, N.H. Oono, K. Sakamoto, M. Hirai, J. Nucl. Mater. **502**, 228 (2018)
[6] S.J. Zinkle, G.S. Was, Acta Mater. **61**, 735 (2013)
[7] Z. Zhang, W. Pantleon, Acta Mater. **149**, 235 (2018)
[8] Q. Zhao, L. Yu, Y. Liu, Y. Huang, Q. Guo, H. Li, J. Wu, Powder Technol. **311**, 449 (2017)
[9] C. Suryanarayana, E. Ivanov, Adv. Powder Metall. **3**, 42 (2013)
[10] Z. Hong, X. Zhang, Q. Yan, Y. Chen, J. Alloys Compd. **770**, 831 (2019)
[11] L.K. Mansur, A.F. Rowcliffe, R.K. Nanstad, S.J. Zinkle, W.R. Corwin, R.E. Stoller, J. Nucl. Mater. **329–333**, 166 (2004)
[12] J.R. Rieken, I.E. Anderson, M.J. Kramer, G.R. Odette, E. Stergar, E. Haney, J. Nucl. Mater. **428**, 65 (2012)
[13] E. Gil, J. Cortés, I. Iturriza, N. Ordás, Appl. Surf. Sci. **427**, 182 (2018)
[14] E. Gil, N. Ordás, C. García-Rosales, I. Iturriza, Fusion Eng. Des. **98–99**, 1973 (2015)
[15] J. Li, S. Wu, P. Ma, Y. Yang, E. Wu, L. Xiong, S. Liu, Mater. Sci. Eng. A **757**, 42 (2019)
[16] R.J. Miller, A. Gangulee, J. Vac. Sci. Technol. **15**, 244 (1978)
[17] K. Nakamura, M. Kamoshida, J. Appl. Phys. **48**, 5349 (1977)
[18] C.M. Wang, G.S. Cargill, H.M. Chan, M.P. Harmer, Acta Mater. **48**, 2579 (2000)
[19] A.M. Thompson, K.K. Soni, H.M. Chan, M.P. Harmer, D.B. Williams, J.M. Chabala, R. Levi-Setti, J. Am. Ceram. Soc. **80**, 373 (1997)

[20] C.L. Briant, K.L. Luthra, Metall. Trans. A **19 A**, 2099 (1988)
[21] J. Wang, S. Liu, X. Bai, X. Zhou, X. Han, Vacuum **173**, 109144 (2020)
[22] C.L. Briant, R.A. Mulford, Metall. Trans. A **13**, 745 (1982)
[23] L.P.H. Jeurgens, W.G. Sloof, F.D. Tichelaar, E.J. Mittemeijer, Surf. Sci. **506**, 313 (2002)
[24] S. Wu, J. Li, W. Li, S. Liu, J. Alloys Compd. **814**, 152282 (2020)
[25] C.L. Chen, Y.M. Dong, Mater. Sci. Eng. A **528**, 8374 (2011)
[26] K. Nomura, Y. Ujihira, J. Mater. Sci. **25**, 1745 (1990)
[27] T. Kosaka, S. Suzuki, H. Inoue, M. Saito, Y. Waseda, E. Matsubara, Appl. Surf. Sci. **103**, 55 (1996)
[28] G. Betz, G.K. Wehner, L. Toth, A. Joshi, J. Appl. Phys. **45**, 5312 (1974)
[29] M. Medraj, R. Hammond, M.A. Parvez, R.A.L. Drew, W.T. Thompson, J. Eur. Ceram. Soc. **26**, 3515 (2006)
[30] D. Pazos, M. Suárez, A. Fernández, P. Fernández, I. Iturriza, N. Ordás, Fusion Eng. Des. **146**, 2328 (2019)
[31] K. Dawson, S.J. Haigh, G.J. Tatlock, A.R. Jones, J. Nucl. Mater. **464**, 200 (2015)